

Diffusion Tensor Image Registration Using Hybrid Connectivity and Tensor Features

Qian Wang,^{1,2,3} Pew-Thian Yap,² Guorong Wu,² and Dinggang Shen^{2,4*}

¹Med-X Research Institute, Shanghai Jiao Tong University, Shanghai

²Department of Radiology and BRIC, University of North Carolina at Chapel Hill, Chapel Hill, North Carolina

³Department of Computer Science, University of North Carolina at Chapel Hill, Chapel Hill, North Carolina

⁴Department of Brain and Cognitive Engineering, Korea University, Seoul, Korea

Abstract: Most existing diffusion tensor imaging (DTI) registration methods estimate structural correspondences based on voxelwise matching of tensors. The rich connectivity information that is given by DTI, however, is often neglected. In this article, we propose to integrate complementary information given by connectivity features and tensor features for improved registration accuracy. To utilize connectivity information, we place multiple anchors representing different brain anatomies in the image space, and define the connectivity features for each voxel as the geodesic distances from all anchors to the voxel under consideration. The geodesic distance, which is computed in relation to the tensor field, encapsulates information of brain connectivity. We also extract tensor features for every voxel to reflect the local statistics of tensors in its neighborhood. We then combine both connectivity features and tensor features for registration of tensor images. From the images, landmarks are selected automatically and their correspondences are determined based on their connectivity and tensor feature vectors. The deformation field that deforms one tensor image to the other is iteratively estimated and optimized according to the landmarks and their associated correspondences. Experimental results show that, by using connectivity features and tensor features simultaneously, registration accuracy is increased substantially compared with the cases using either type of features alone. *Hum Brain Mapp* 35:3529–3546, 2014. © 2013 Wiley Periodicals, Inc.

Key words: diffusion tensor image registration; connectivity features; tensor features; correspondence detection

INTRODUCTION

This article was published online on 30 November 2013. An error was subsequently identified. This notice is included in the online and print versions to indicate that both have been corrected 25 March 2014.

*Correspondence to: Dinggang Shen, Department of Radiology and BRIC, University of North Carolina at Chapel Hill, 130 Mason Farm Road, Chapel Hill, NC 27599. E-mail: dgshen@med.unc.edu
Received for publication 26 July 2013; Revised 23 September 2013; Accepted 27 September 2013.

DOI 10.1002/hbm.22419

Published online 30 November 2013 in Wiley Online Library (wileyonlinelibrary.com).

Diffusion tensor imaging (DTI) [Basser et al., 1994] provides a noninvasive way to probe the anisotropic water diffusion patterns that are shaped by the architectures of brain tissue microstructures. It has triggered enormous interest in related researches for the last decades. However, comparison of DTI data across individual subjects is often hindered by improper alignment of brain structures. Inaccurate registration of diffusion tensor (DT) images causes analyses to be erroneously performed based on mismatched structures, leading to conclusions that are questionable. While accurate DTI registration methods are clearly desirable, advancements in this direction are challenged by the task of determining

image features that can effectively guide alignment of microstructures in DT images.

Several DTI registration methods have been reported in the literature. Tensors, due to their higher dimensionality, are significantly more difficult to handle than scalar data. The associated difficulty in evaluating tensor similarity and determining tensor correspondence poses a major challenge to DTI registration [Gee and Alexander, 2006]. To this end, an intuitive and straightforward solution is to adapt scalar image registration techniques for use with DT images. Park et al. [2003], for instance, combine several channels of scalar descriptors for each voxel (including T2-weighted image intensity, fractional anisotropy, trace of tensor, eigenvalues, etc.), and then apply the multichannel Demons algorithm to estimate the deformation field between two DT images. A similar strategy is also applied in Guimond et al. [2002]. Other approaches consider the entire tensor when detecting correspondences between images [Alexander and Gee, 2000; Yan et al., 2006]. For example, Ruiz-Alzola et al. [2002] optimized the tensor similarity between tensor images in regions with high structural information and generated the deformation field using kriging interpolation. Zhang et al. [2006] performed matching based on the full tensor and explicitly take into account the tensor re-orientation during optimization. Yeo et al. [2008] developed a fast diffeomorphic DTI registration algorithm by computing the differential of the finite strain (FS) re-orientation with respect to the Jacobian. Other similarity- or dissimilarity-measures for DTI registration include mutual information (MI) [Rohde et al., 2003; van Hecke et al., 2007], symmetrized Kullback-Leibler (sKL) divergence [Chiang et al., 2008], and Geodesic-Loxodromes [Irfanoglu et al., 2008].

Similar to scalar image registration, feature-based registration [Wu et al., 2006; Zacharaki et al., 2008; Shen et al., 1999] provides an effective alternative in registering DTI data. A feature vector, formed from multiple attributes of a voxel, can better describe the voxel and help reduce matching ambiguities in searching for its correspondence. The improved voxel correspondences thus contribute to estimating a more accurate deformation field [Jia et al., 2011; Verma and Davatzikos, 2004]. Yang et al. [2008], for instance, use prolateness, oblateness, and sphericity as tensor attributes. A more recent method, TIMER [Yap et al., 2009], as well as its improved variant F-TIMER [Yap et al., 2010], characterizes each voxel using statistical features of the voxel neighborhood. These features include the principal diffusivities (PDs) of each tensor, PDs of the mean/variance tensor in the neighborhood, and the fractional anisotropy (FA). For better alignment of white matter structures, a set of distinctive landmarks is automatically selected from the edges of both the tensor field and the fractional anisotropy (FA) image to help guide correspondence detection.

DTI reveals water molecule diffusion patterns in brain tissues and provides a unique insight into brain connectivity. By utilizing tractography techniques, for example, researchers are able to delineate neural pathways that carry signals between individual brain anatomies [Mori

and van Zijl, 2002]. The rich connectivity information conveyed by DTI data can potentially be harnessed to improve registration involved with DT images [Ingallhalikar et al., 2010; Li et al., 2009; Siless et al., 2012]. An early effort to incorporate connectivity information into DTI registration by Goodlett et al. [2006] applied a carefully designed stencil on the FA map to detect fiber bundles as tubular or sheet-like structures, from which features are derived to encode connectivity information and further steer registration. Ziyan et al. [2007] applied automatic tractography clustering to individual datasets and establish correspondences between fiber bundles. They then utilize the detected bundle correspondences for registration and further model the deformation field between the two DT images by polyaffine transformations. Although these methods demonstrate that the connectivity information is conducive to improve DTI registration, they unfortunately ignore the important tensor information.

To efficiently combine both brain connectivity and local tensor information for DTI registration, we previously proposed a two-stage sequential registration framework in Wang et al. [2011]. In the first *tract-guided* stage, we use connectivity features derived from neural tracts to generate a coarse estimation of the low-resolution deformation field. In the second *tensor-guided* stage, the deformation is refined at high resolution by using tensor-derived features [Yap et al., 2010]. To generate the connectivity features at the first stage, we label several seed regions to indicate core areas of individual major neural tracts in the brain and then grow the seed regions along fibers identified by tractography. The growing of each seed region results in certain *bundle pattern*, which spans the whole brain. The combination of bundle patterns defines the connectivity features for each voxel. As we have shown in Wang et al. [2011], connectivity features and tensor features carry complementary information that describes brain structures at different scales, thus benefiting registration by integrating both of them. However, the two-stage design of Wang et al. [2011] separates the contributions of connectivity and tensor features into different stages. Specifically, the connectivity information is restricted within low-resolution registration only, while the counterpart tensor features act their roles only in the high-resolution stage. The arbitrary separation undermines the capability to exploit both types of features to further improve DTI registration.

To address the limitations in Wang et al. [2011], we present a new DTI registration framework utilizing connectivity and tensor features simultaneously for the estimation of voxelwise correspondences in an adaptive fashion. In particular, we generate the connectivity features by automatically placing two sets of corresponding *anchors* in the image spaces of both the template and the subject, respectively. We then evaluate the geodesic distance, with respect to the tensor field, from an anchor to every voxel by using fast marching [Sethian, 1996]. For each voxel, the connectivity features consist of the distance measures from all anchors to the voxel itself, which can be

used to tell the voxel apart from others. At the same time, we employ tensor features that reflect the local statistics within the neighborhood of each voxel [Yap et al., 2010]. A set of landmarks that is crucial to accurate DTI registration is then selected. Each landmark seeks for its correspondence that is most similar to the landmark according to their extracted features. For increased robustness, we adopt the soft correspondence strategy [Chui and Rangarajan, 2003], where each landmark is assigned probabilistically to multiple matching candidates of correspondences. By refining correspondence information of the selected landmarks iteratively, the deformation field that warps the subject to the template can be obtained. After warping the subject to the template space, we finally re-orient the tensors based on the principal diffusion directions for achieving consistency of local connectivity pattern [Xu et al., 2003].

Major improvements in the new method include:

1. In contrast to our previous work in Wang et al. [2011], both the connectivity features and the tensor features are utilized for the estimation of the deformation field simultaneously. The resolution barrier between the two types of features in contributing to registration is removed.
2. Besides calculating the connectivity features more precisely and efficiently, we propose an adaptive weighting mechanism that focuses only on reliable entries in the connectivity feature vector. The new strategy improves the accuracy in evaluating voxel similarity in terms of connectivity features, thus leading to more reliable correspondence detection for landmarks.
3. We rely on automatically selected landmarks and their associated correspondence information to estimate the deformation field in DTI registration. The new matching scheme of the proposed algorithm can better utilize all voxel features, compared with Wang et al. [2011], to enhance registration performances.

In what follows, we detail the proposed method and demonstrate its performances. The connectivity features and the tensor features are introduced in “Connectivity Features and Tensor Features” section, while the design of the registration framework that utilizes both features simultaneously is described in “Registration Framework” section. We show that the new method can improve registration performances substantially in “Experimental Results” section, followed by “Conclusion and Discussion” section.

CONNECTIVITY FEATURES AND TENSOR FEATURES

The objective of this work is to simultaneously employ connectivity features and tensor features for DTI registration. Well-performing features are essentially important to the proposed method. Thus, in the next, we will describe how both types of features are to be computed.

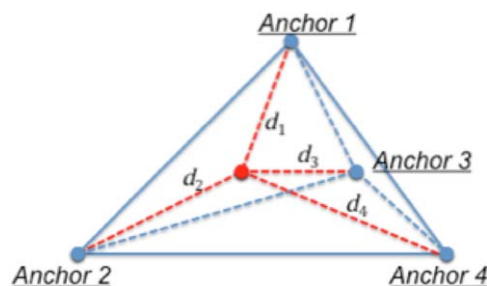


Figure 1.

Given four fixed anchors (blue, d_1 to d_4), the unique location for a point (red) in the three-dimensional Euclidean space can be determined if its distances to the anchors are known. [Color figure can be viewed in the online issue, which is available at wileyonlinelibrary.com.]

Connectivity Features

The term *connectivity* refers to the spatial relationship between voxels in the context of brain tissue diffusivity. Assuming that a number of *anchors* have been placed in the image space, we define the connectivity features of each voxel as the geodesic distances from all anchors to the voxel under consideration. For the voxel x , the measurements of the distances are arranged into the *connectivity feature vector* $\vec{c}(x)$, where each entry corresponds to an individual anchor. We further argue that the connectivity features are capable to identify a specific voxel from others. In Figure 1, for example, the unique position of the red point in 3D Euclidean space can be determined with respect to (up to) four fixed anchors that are colored in blue, once the distance from the red point to each anchor (i.e., d_1 to d_4) are known. In other words, the distances between the anchors and the red point, or the connectivity features for the red point, represent a unique descriptor of the location of the point.

Given a voxel in the template image and its correspondence in the subject space, the similarity between their connectivity features is expected to be high [Wang et al., 2011]. To guarantee that the connectivity features are practically feasible and the evaluation of feature similarity is precise, we need to tackle two issues: (1) placement of anchors and (2) calculation of distances from the anchors to each voxel. Since the template voxel under consideration and its subject correspondence are located in the two different image spaces, their connectivity features are acquired by referring to a different set of anchors for each image space. The in-between correspondences of the two sets of anchors in both the template and the subject spaces are required, in order to assure that the connectivity features of the two voxels under consideration are comparable, even though the two anchor sets are placed independently.

For robustness against possible errors in anchor placement, multiple anchors are deployed in both the template and the subject image spaces. The placement of anchors is guided by brain anatomy to assure approximate

correspondences between pairs of anchors in each image. On basis of these automatically placed anchors, we then compute the connectivity features, which are composed by the geodesic distances from all anchors to the voxels, as determined by the connectivity information provided by the tensor fields. To further alleviate influences from the wrongly placed anchors, we select a subset of anchors whose correspondences are more reliable and assign to them with varying weights prior to evaluating the similarity upon connectivity features of individual voxels. The similarity between two voxels in the template and the subject images can finally be calculated according to their weighted connectivity features.

Anchor placement

It is necessary to maintain (approximate) correspondences between pairs of anchors in the template and the subject images. Though manual placement of landmarks provides a possible solution, such a task becomes intractable for large datasets. Therefore, we adopt an automated approach guided by brain anatomy for landmark placement. Specifically, we first register the JHU-EVE atlas [Mori et al., 2008] (hereafter referred to as the *atlas*) to the template and subject images independently by aligning the FA maps via affine scalar image registration (i.e., FLIRT [Jenkinson and Smith, 2001] followed by diffeomorphic Demons [Vercauteren et al., 2009]). On the basis of estimated deformations, we then warp the white matter parcellation map (WMPM) that comes with the atlas to parcellate the template and subject images. Of 130 available ROIs labeled by the atlas, we use 52 cortical regions (including their adjacent superficial whiter matter areas) and 56 deep white matter regions [Mori et al., 2008]. These ROIs are associated with the pathways of brain white matter tracts, thus enabling us to investigate the connectivity information from them to other voxels. To represent each warped ROI, we further define the anchor as the center of gravity of the ROI weighted by the FA values within the ROI. In associating an anchor with an ROI, we are able to correlate the anchor with a specific anatomical meaning. Thus we have established approximate correspondences between pairs of anchors across the template and the subject.

Connectivity feature calculation

To obtain the connectivity features for a certain voxel, we need to calculate the geodesic distances from all anchors to the voxel in the context of the tensor field. We assume that each anchor is tightly encircled by a closed interface. Then, we apply the fast marching [Sethian, 1996] method to propagate the interface outward by referring to the tensor field. The propagation expands the volume inside the interface, as more voxels are gradually swamped by the evolving interface. This process of anisotropic propagation eventually results in a time arrival map, which records the time that the interface takes to depart from its starting position and

reach each individual voxel. The time value associated with each voxel is taken as the geodesic distance from the specific anchor to the voxel.

The time arrival map in fast marching is generated by solving the Eikonal equation $v\nabla\tau=1$ in the image space. Here v indicates the velocity of the anisotropic propagation on the interface, and τ records the time that the interface takes to arrive at a specific location. Similar to Wang et al. [2012], the propagation is constrained to be always perpendicular to the evolving interface, or parallel to the surface normal. However, in contrast to Wang et al. [2012], we derive the velocity v from the tensor field to reflect brain connectivity directly. Denoting the interface unit normal as \vec{n} and the local tensor as \mathbf{W} , we define $v=\vec{n} \cdot \mathbf{W} \cdot \vec{n}$ and then update a local patch of the time arrival map accordingly. To prevent the interface from entering low-FA regions where connectivity information is unreliable, the propagation velocity v is set to zero if the FA value drops below 0.2. We have implemented the high-order 3D lattice operator [Bærentzen, 2001] and the multistencil strategy [Hassouna and Farag, 2007] for more efficient and accurate computation of the time arrival map in fast marching.

The procedure above is performed independently on the 108 (=52 + 56) anchors to generate their individual time arrival maps. Note that all datasets (including both template and subject) are linearly aligned already by applying affine registration to their FA maps. As the result, the scale issue of the template and the subject images is not necessary to be considered in the stage of deformable registration. We also require the propagation process to abort only when the interface has encircled all possible volume (i.e., with FA values higher than the designated threshold) in the image space. After the time arrival maps are rescaled to the range [0,1] independently, the connectivity features of two voxels in the template and the subject are comparable with respect to two sets of anchors underlined by identical anatomies, that is, the same set of ROIs.

For each voxel, we collect a connectivity feature vector, where each entry corresponds to the rescaled geodesic distance from a specific anchor to the voxel. Figure 2 shows examples of the time arrival maps with respect to two anchors. The first row of Figure 2 shows five consecutive FA slices from a DTI dataset. The anchor representing the right superior frontal gyrus (R-SFG) and its time arrival map are shown in Figure 2B. In Figure 2C, we show the results for the anchor associated with the left superior frontal gyrus (L-SFG). All features combined allow us to evaluate the similarity between two voxels.

Similarity evaluation of connectivity features

We define the two sets of anchors as $\mathbb{Z}^T=\{\mathbf{z}_i^T, i=1, \dots, M\}$ in the template image space and $\mathbb{Z}^S=\{\mathbf{z}_i^S, i=1, \dots, M\}$ in the subject space. The connectivity feature vector for the voxel \mathbf{x} in the template is denoted by $\vec{c}(\mathbf{x})=\{c_{\mathbf{x},i}, i=1, \dots, M\}$, where $c_{\mathbf{x},i}$ corresponds to the entry

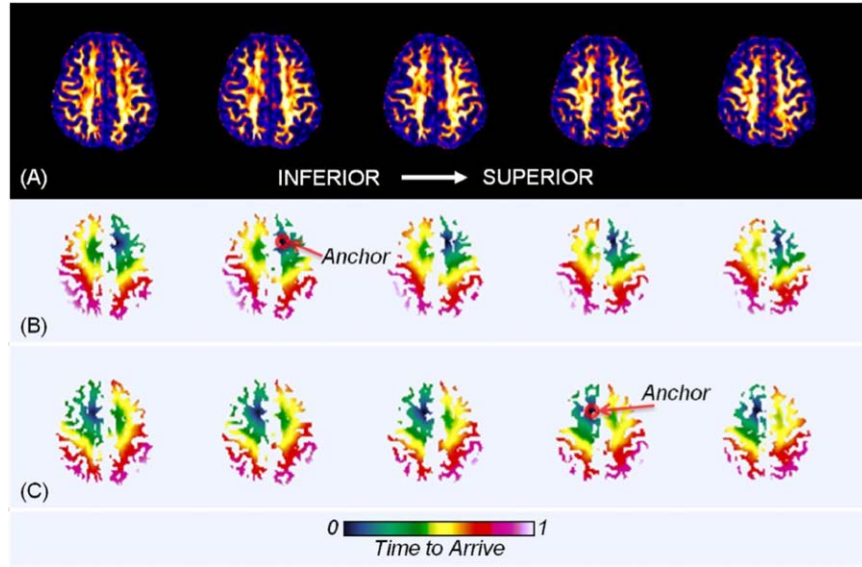


Figure 2.

(A) Five consecutive FA slices from a single DT image. Time arrival maps with respect to (B) right superior frontal gyrus (R-SFG) and (C) left superior frontal gyrus (L-SFG). Both anchors are marked by arrows. [Color figure can be viewed in the online issue, which is available at wileyonlinelibrary.com.]

associated with \mathbf{z}_i^T in the template space. Similarly, the counterpart feature vector for the voxel $\hat{\mathbf{x}}$ in the subject space, which is the correspondence to \mathbf{x} , is signified by its feature vector $\tilde{\mathbf{c}}(\hat{\mathbf{x}}) = \{c_{\hat{\mathbf{x}},i}, i=1, \dots, M\}$. As all entries in the feature vectors are scaled and comparable, the similarity between the connectivity features of voxels \mathbf{x} and $\hat{\mathbf{x}}$ can be simply calculated as $-\|\tilde{\mathbf{c}}(\mathbf{x}) - \tilde{\mathbf{c}}(\hat{\mathbf{x}})\|^2$. This similarity evaluation, however, suffers from two drawbacks: (1) all entries are treated equally while the reliability of the correspondences between certain pairs of anchors is questionable; and (2) the lengthy feature vector causes high but redundant computational loads. For example, an anchor representing the gravity center for a certain ROI can possibly be placed into low-FA (i.e., $\text{FA} < 0.2$) area such that the associated connectivity features are non-helpful to voxel similarity evaluation and image registration. As a remedy, we adopt the following adaptive weighting strategy, illustrated in Figure 3, for more accurate voxel similarity evaluation upon the connectivity features.

We aim to estimate the posterior probability $p(\mathbf{x}, \hat{\mathbf{x}} | \tilde{\mathbf{c}}(\mathbf{x}), \tilde{\mathbf{c}}(\hat{\mathbf{x}}))$. The reliability, or the confidence, of the correspondence between \mathbf{x} and $\hat{\mathbf{x}}$ is related to the agreement of their connectivity features $\tilde{\mathbf{c}}(\mathbf{x})$ and $\tilde{\mathbf{c}}(\hat{\mathbf{x}})$. It is worth noting that, for a specific pair of anchors in the subject and the template images, the confidence of their in-between correspondence is assumed to be independent of all other pairs of anchors. That is, $p(\mathbf{z}_i^T, \mathbf{z}_i^S)$ is independent of $p(\mathbf{z}_j^T, \mathbf{z}_j^S)$. Moreover, we avoid imposing any arbitrary priors to anchors and the connectivity features, as the potential errors in placing individual anchors are largely unknown.

For a given template voxel \mathbf{x} and its correspondence $\hat{\mathbf{x}}$ in the subject (both indicated by red dots in Fig. 3), only entries $c_{\mathbf{x},i}$ and $c_{\hat{\mathbf{x}},i}$ in their connectivity feature vectors are related with the specific i -th pair of anchors \mathbf{z}_i^T and \mathbf{z}_i^S (both as green colored dots). As the result, we are capable to acquire $p(c_{\mathbf{x},i}, c_{\hat{\mathbf{x}},i} | \mathbf{x}, \hat{\mathbf{x}}, \mathbf{z}_i^T, \mathbf{z}_i^S)$ as

$$\begin{aligned} p(c_{\mathbf{x},i}, c_{\hat{\mathbf{x}},i} | \mathbf{x}, \hat{\mathbf{x}}, \mathbf{z}_i^T, \mathbf{z}_i^S) &= \frac{p(c_{\mathbf{x},i}, c_{\hat{\mathbf{x}},i}, \mathbf{x}, \hat{\mathbf{x}}, \mathbf{z}_i^T, \mathbf{z}_i^S)}{p(\mathbf{x}, \hat{\mathbf{x}}, \mathbf{z}_i^T, \mathbf{z}_i^S)} \\ &= \frac{p(c_{\mathbf{x},i}, c_{\hat{\mathbf{x}},i}, \mathbf{x}, \hat{\mathbf{x}})}{p(\mathbf{x}, \hat{\mathbf{x}})} \cdot \frac{p(c_{\mathbf{x},i}, c_{\hat{\mathbf{x}},i}, \mathbf{z}_i^T, \mathbf{z}_i^S)}{p(\mathbf{z}_i^T, \mathbf{z}_i^S)} \quad (1) \\ &= p(c_{\mathbf{x},i}, c_{\hat{\mathbf{x}},i} | \mathbf{x}, \hat{\mathbf{x}}) \cdot p(c_{\mathbf{x},i}, c_{\hat{\mathbf{x}},i} | \mathbf{z}_i^T, \mathbf{z}_i^S). \end{aligned}$$

The equation above is valid in that the confidences related with \mathbf{x} , $\hat{\mathbf{x}}$ and \mathbf{z}_i^T , \mathbf{z}_i^S are independent. Intuitively, the probability $p(c_{\mathbf{x},i}, c_{\hat{\mathbf{x}},i} | \mathbf{x}, \hat{\mathbf{x}}, \mathbf{z}_i^T, \mathbf{z}_i^S)$ captures the disagreement between $c_{\mathbf{x},i}$ and $c_{\hat{\mathbf{x}},i}$, both of which are observable connectivity features for \mathbf{x} and $\hat{\mathbf{x}}$. Given \mathbf{x} , $\hat{\mathbf{x}}$ and \mathbf{z}_i^T , \mathbf{z}_i^S as two respective pairs of well-determined correspondences, the disagreement of $c_{\mathbf{x},i}$ and $c_{\hat{\mathbf{x}},i}$ is expected to vanish. Therefore, we further use a simple Gaussian to empirically model the disagreement between $c_{\mathbf{x},i}$ and $c_{\hat{\mathbf{x}},i}$ as

$$p(c_{\mathbf{x},i}, c_{\hat{\mathbf{x}},i} | \mathbf{x}, \hat{\mathbf{x}}, \mathbf{z}_i^T, \mathbf{z}_i^S) = \exp\left(-\frac{(c_{\mathbf{x},i} - c_{\hat{\mathbf{x}},i})^2}{2\sigma^2}\right), \quad (2)$$

where σ can be calculated as the standard deviation (STD) of the errors between all observable pairs of $c_{\mathbf{x},i}$ and $c_{\hat{\mathbf{x}},i}$.

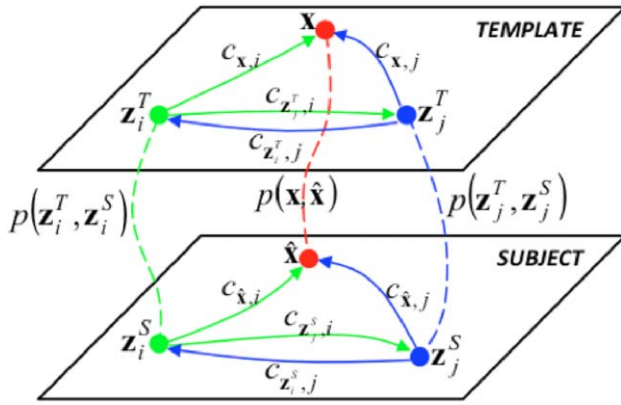


Figure 3.

Illustration of calculating the confidence for each pair of anchors. The error between connectivity features $c_{x,i}$ for \mathbf{x} and $c_{\hat{x},i}$ for $\hat{\mathbf{x}}$ depends on (1) $p(z_i^T, z_i^S)$ that indicates the confidence of the correspondence between anchors z_i^T and z_i^S ; (2) $p(\mathbf{x}, \hat{\mathbf{x}})$ that indicates the confidence of the correspondence between voxels \mathbf{x} and $\hat{\mathbf{x}}$. [Color figure can be viewed in the online issue, which is available at wileyonlinelibrary.com.]

From Figure 3, we conclude intuitively that the disagreement between $c_{x,i}$ and $c_{\hat{x},i}$ is dependent on (1) the confidence of the correspondence between z_i^T and z_i^S (indicated by the green dashed curve); and (2) the correspondence confidence between \mathbf{x} and $\hat{\mathbf{x}}$ (indicated by the red dashed curve). The conclusion can also be drawn from the maximum-likelihood (ML) setting according to the Bayesian rule. By ignoring priors to individual anchors and their associated connectivity features, we have

$$p(\mathbf{x}, \hat{\mathbf{x}} | \vec{c}(\mathbf{x}), \vec{c}(\hat{\mathbf{x}})) \propto p(\vec{c}(\mathbf{x}), \vec{c}(\hat{\mathbf{x}}) | \mathbf{x}, \hat{\mathbf{x}}) \propto p(c_{x,i}, c_{\hat{x},i} | \mathbf{x}, \hat{\mathbf{x}}). \quad (3)$$

We further regard $p(c_{x,i}, c_{\hat{x},i} | \mathbf{x}, \hat{\mathbf{x}})$ as an observed measure toward to the to-be-estimated confidence $p(\mathbf{x}, \hat{\mathbf{x}} | \vec{c}(\mathbf{x}), \vec{c}(\hat{\mathbf{x}}))$.

By combining Eqs. (1) and (2), plugging Eq. (3) to the right side of Eq. (1), and replacing \mathbf{x} , $\hat{\mathbf{x}}$ with another pair of anchors z_i^T, z_j^S ($j \neq i$) (blue in Fig. 3), immediately we have the following

$$p(z_i^T, z_j^S | \vec{c}(z_i^T), \vec{c}(z_j^S)) \cdot p(z_i^T, z_j^S | \vec{c}(z_i^T), \vec{c}(z_j^S)) = \exp\left(-\left(c_{z_i^T, j} - c_{z_j^S, i}\right)^2 / 2\sigma^2\right). \quad (4)$$

It is worth noting that the symmetric form of Eq. (4) is slightly different due to the nonclosed form in evaluating connectivity features (c.f., green and blue arrows between z_i^T and z_j^S , as well as z_j^T and z_i^S). In particular, we have

$$p(z_i^T, z_j^S | \vec{c}(z_i^T), \vec{c}(z_j^S)) \cdot p(z_j^T, z_i^S | \vec{c}(z_j^T), \vec{c}(z_i^S)) = \exp\left(-\left(c_{z_i^T, j} - c_{z_j^S, i}\right)^2 / 2\sigma^2\right). \quad (5)$$

After denoting $q_i = \log p(z_i^T, z_j^S | \vec{c}(z_i^T), \vec{c}(z_j^S))$, we then rewrite Eqs. (4) and (5) as

$$\begin{aligned} q_i + q_j &= -\left(c_{z_i^T, j} - c_{z_j^S, i}\right)^2 / 2\sigma^2, \\ q_j + q_i &= -\left(c_{z_j^T, i} - c_{z_i^S, j}\right)^2 / 2\sigma^2. \end{aligned} \quad (6)$$

Equation (6) finally yields the overcomplete linear system that incorporates all pairs of i and j . In order to estimate the optimal q_i and its equivalent $p(z_i^T, z_j^S | \vec{c}(z_i^T), \vec{c}(z_j^S))$, we have followed the least-square rule. That is, from Eq. (6), we conclude that q_i and q_j should satisfy the relaxed symmetric constraint

$$q_i + q_j = \left[-\left(c_{z_i^T, j} - c_{z_j^S, i}\right)^2 / 2\sigma^2 - \left(c_{z_j^T, i} - c_{z_i^S, j}\right)^2 / 2\sigma^2 \right] / 2. \quad (7)$$

Then, we aim to solve the following optimization problem

$$\begin{aligned} \{q_i^*\} &= \arg \min_{\{q_i\}} \sum_{i,j=1,\dots,M} \left(q_i + q_j + \frac{\left(c_{z_i^T, j} - c_{z_j^S, i}\right)^2 + \left(c_{z_j^T, i} - c_{z_i^S, j}\right)^2}{4\sigma^2} \right)^2 - \gamma \sum_{i,j=1,\dots,M} |q_i|, \\ \text{s.t. } q_i &\leq 0, \forall i. \end{aligned} \quad (8)$$

The first term in Eq. (8) reflects the equality constraint in Eq. (7). We have appended the ℓ_1 -norm regularization term $-\gamma \sum_{i=1,\dots,M} |q_i|$ in order to penalize the number of anchors whose calculated confidences are high. By increasing the positive scalar γ , fewer anchors remain effective, in turn causing the connectivity feature vector to become sparser. In this way, only reliable anchors will be preserved as active, and the computational loads in estimating voxel similarities will then be reduced. Generally, the

optimization problem in Eq. (8) can be solved via quadratic programming, for which we use CVXOPT¹. After the confidence of every pair of anchors has been calculated, we finally define the weighted similarity between voxels \mathbf{x} and $\hat{\mathbf{x}}$ in terms of their connectivity features as

¹The CVXOPT distribution is accessible at <http://abel.ee.ucla.edu/cvxopt>.

$$S_c(\mathbf{x}, \hat{\mathbf{x}}) = - \sum_i (c_{\mathbf{x},i} - c_{\hat{\mathbf{x}},i})^2 \exp q_i. \quad (9)$$

Tensor Features

Besides the connectivity features introduced above, we incorporate tensor features directly for accurate DTI registration. We use the tensor features applied in Yap et al. [2009, 2010], which are comprised of three parts, including regional features, geometrical features, and edge features:

- The *regional features* account for the appearances of tensors for a certain voxel and its neighbors. They are calculated as the eigenvalues, or principal diffusivities (PDs), of the mean and the variance tensors computed using the Log-Euclidean metric [Arsigny et al., 2006] from the tensors in the neighborhood of the centered voxel.
- The *geometrical features* focus on the individual tensors. They consist of the FA and PDs (in descending order) of the tensor for a given location.
- Extracting edge information is crucial for accurate alignment of tissue boundaries. Two types of edges, one directly from tensors, and the other from the FA map, are extracted to produce the *edge features*. The Canny operator is used for detection of both types of edges. The tensor edges are acquired using the logarithmic space [Arsigny et al., 2006]. More details on the detection of tensor edges and FA edges can be found in Yap et al. [2009].

We normalize each entry in the tensor feature vector to the range [0,1] independently. Thus, all entries of the tensor features are comparable and can be equally treated. In particular, for the template voxel \mathbf{y} and its correspondence $\hat{\mathbf{y}}$ in the subject space, we denote their tensor feature vectors as $\vec{t}(\mathbf{y})$ and $\vec{t}(\hat{\mathbf{y}})$, respectively. Then, the similarity between the two voxels \mathbf{y} and $\hat{\mathbf{y}}$ in terms of their tensor features is computed as

$$S_t(\mathbf{y}, \hat{\mathbf{y}}) = - \|\vec{t}(\mathbf{y}) - \vec{t}(\hat{\mathbf{y}})\|^2. \quad (10)$$

REGISTRATION FRAMEWORK

Given the connectivity features and tensor features, we are able to evaluate similarities between voxels and identify voxel correspondences. The detected voxel correspondences between the template and the subject are then utilized for the estimation of the deformation field that warps the moving subject to the space of the fixed template. The deformed tensors are re-oriented in the final step to achieve consistent structures for local connectivity [Xu et al., 2003].

To design an efficient registration framework, we follow the widely applied iterative matching strategy in feature-

based registration similar to Yap et al. [2009, 2010]. In every iteration, we first select a subset of voxels as landmarks that are crucial to accurate registration of DT images. Correspondences of the selected landmarks are then detected according to their calculated features. On the basis of selected landmarks and their tentative correspondences, we are able to estimate a dense incremental field that refines the overall deformation field iteratively. The procedure above is repeated until that the overall deformation field can accurately warp the subject image to the template.

Selection of Landmarks

Although multiple features provide better capabilities to characterize individual voxels, it is still challenging to identify correspondences for all voxels in the image space. Moreover, the computational load that comes with correspondence detection for every voxel can also be formidable. With these constraints in mind, we select a subset of landmark voxels in our method and restrict correspondence detection to the selected landmarks only. The subset of selected landmarks consists of voxels that are most important to image registration, thus helping to estimate a reliable deformation field. The limited size of the landmark subset, compared with the size of the images to be registered, also significantly reduces computational loads.

We argue that the most important voxels to image registration are located at transitions of image textures, or *edges* of features. As the result, a voxel is more likely to be selected as a landmark if (1) the possibility that the voxel lays on feature edges is higher or (2) the voxel is closer to the edges. In order to select landmarks, we use the Canny operator to detect feature edges for both the template and the subject images. Specifically, we apply Canny edge detection on a map, which is created by integrating all entries in the connectivity feature vector, to detect the edges of connectivity features. For tensor features, the accompanying edge information, which consists of FA edge and tensor edge, has been computed as parts of the tensor feature vector described in “Tensor Features” section. The magnitudes of edge responses from Canny edge detection are then smoothed in the Gaussian manner to indicate the likelihoods of individual voxels for being qualified as landmarks. Finally, we apply the random sampling strategy [Wang et al., 2010] to collect enough landmarks according to their likelihoods.

We show an example slice of the landmark likelihoods associated with connectivity features in Figure 4B. The corresponding landmarks, referred to as *C-type* landmarks, are colored in red in Figure 4A. The counterpart blue landmarks in Figure 4A are selected based on their relationship with edges from the tensor feature vector. Therefore, we refer to these as *T-type* landmarks. The likelihoods for determining the T-type landmarks are shown in Figure 4C,D. In particular, Figure 4C depicts smoothed edge

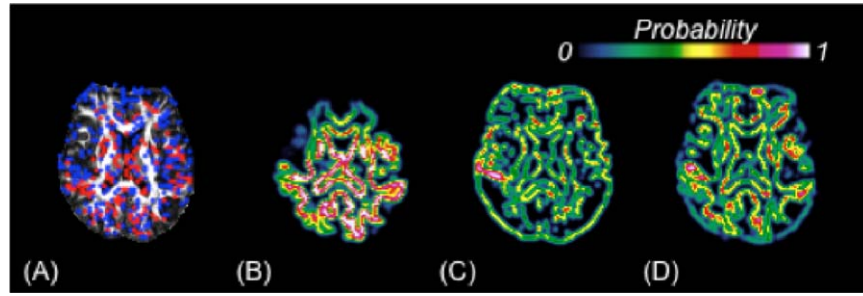


Figure 4.

C-type landmarks and T-type landmarks are colored in red and blue, respectively, in (A). The C-type landmarks are randomly sampled according to the likelihoods in (B), which is related to edge responses from the connectivity features. The T-type landmarks are sampled from the likelihood maps in (C) and (D), which correspond to FA edges and tensor edges, respectively. [Color figure can be viewed in the online issue, which is available at wileyonlinelibrary.com.]

responses from FA values, while Figure 4D is for the tensor edges. The number of both C-type and T-type landmarks in total accounts for $\sim 20\%$ of the brain volume size in the beginning of registration; this percentile gradually increases to $\sim 50\%$ until the registration process terminates. Note that we have down-sampled the subset of landmarks in Figure 4A for clearer visualization.

Estimation of the Deformation Field

The task of image registration is to find the deformation field ϕ that associates the voxel \mathbf{p} in the template space to its correspondence $\hat{\mathbf{p}} = \phi(\mathbf{p})$ in the subject space. The estimated deformation field matches the selected landmarks to their correspondences in terms of the connectivity features and the tensor features. Therefore, we aim to maximize the objective function

$$F(\phi, \mathbb{X}, \mathbb{Y}) = \text{Sim}_{\mathbb{X}}(\mathbb{X}, \phi) + \text{Sim}_{\mathbb{Y}}(\mathbb{Y}, \phi) - \text{Reg}(\phi), \quad (11)$$

where $\mathbb{X} = \{\mathbf{x}_i, i=1, \dots, \mathcal{N}_c\}$ is the set of the C-type landmarks, and $\mathbb{Y} = \{\mathbf{y}_j, j=1, \dots, \mathcal{N}_t\}$ is the set of T-type landmarks. The first term on the right side of Eq. (11) measures the similarities between the C-type landmarks and their correspondences, while the second term accounts for the other T-type landmarks. The two terms evaluate the total similarities contributed from all C-type and T-type landmarks, respectively. In particular, we have

$$\begin{aligned} \text{Sim}_{\mathbb{X}}(\mathbb{X}, \phi) &= \sum_{i=1}^{\mathcal{N}_c} S_c(\mathbf{x}_i, \phi(\mathbf{x}_i)), \\ \text{Sim}_{\mathbb{Y}}(\mathbb{Y}, \phi) &= \sum_{j=1}^{\mathcal{N}_t} S_t(\mathbf{y}_j, \phi(\mathbf{y}_j)), \end{aligned} \quad (12)$$

by using Eqs. (9) and (10). The term $\text{Reg}(\phi)$ in Eq. (11) measures the irregularity of the deformation field and imposes the smoothness constraint that is desirable in image registration.

It is difficult to optimize the objective function in Eq. (11) directly since the problem is under the high dimensional setting. As an alternative, we split the optimization into two iterative steps [Yap et al., 2009, 2010]:

1. Tentatively fix the deformation field ϕ , and update correspondences for landmarks $\{\mathbf{x}_i\}$ and $\{\mathbf{y}_j\}$ by searching for the correspondence of each given landmark in the local neighborhood. We allow detection of *soft correspondences* [Chui and Rangarajan, 2003] between landmarks for greater robustness. This results in an incremental displacement $u(\mathbf{p})$, which assigns the landmark \mathbf{p} to its updated correspondence following $\hat{\mathbf{p}} \leftarrow \phi(\mathbf{p}) + u(\mathbf{p})$.
2. Given the incremental displacements associated with the landmarks, we compute a regularized incremental deformation $\Delta\phi$ and update ϕ following $\phi \leftarrow \phi + \Delta\phi$. The smoothness constraint is imposed when estimating the incremental $\Delta\phi$. The constraint thus results in the fluid-style regularization on the overall deformation field ϕ , which fulfills the smoothness regularization term $\text{Reg}(\phi)$ in Eq. (11).

These two steps will be iterated until convergence when the incremental deformation $\Delta\phi$ vanishes, or when the number of iterations has been exhausted.

Updating the correspondences

Tentatively fixing the deformation field ϕ , the correspondence of a certain C-type landmark \mathbf{x}_i is updated from $\phi(\mathbf{x}_i)$ to the new location $\phi(\mathbf{x}_i) + u(\mathbf{x}_i)$. The incremental displacement $u(\mathbf{x}_i)$ is determined by maximizing the similarity between \mathbf{x}_i and the new correspondence candidate, or simply $S_c(\mathbf{x}_i, \phi(\mathbf{x}_i) + u(\mathbf{x}_i))$. Similarly, we can determine the optimal incremental displacement $u(\mathbf{y}_j)$ for the T-type landmark \mathbf{y}_j as the displacement that maximizes

$S_t(\mathbf{y}_j, \phi(\mathbf{y}_j) + u(\mathbf{y}_j))$. However, the process of assigning the landmark to a single correspondence might be vulnerable to high noise in the image data. As the result, we allow multiple correspondences for each landmark [Chui and Rangarajan, 2003]. We define $p(u|\mathbf{p}, \phi)$ to model the probabilities for the landmark \mathbf{p} to choose its incremental displacement and the accompanying correspondence. The probability is proportional to the gain of the similarity associated with each possible displacement. Moreover, the landmark \mathbf{p} can only search for its correspondence within the neighborhood of $\phi(\mathbf{p})$, implying that higher magnitude of the displacement is less favored and should be penalized. Therefore, we define the probability model $p(u|\mathbf{p}, \phi)$ for both the C-type and the T-type landmarks by

$$\begin{aligned} p(u|\mathbf{x}_i, \phi) &:= S_c(\mathbf{x}_i, \phi(\mathbf{x}_i) + u(\mathbf{x}_i)) \cdot \exp\left(\|u(\mathbf{x}_i)\|^2 / \sigma_N^2\right), \\ p(u|\mathbf{y}_j, \phi) &:= S_t(\mathbf{y}_j, \phi(\mathbf{y}_j) + u(\mathbf{y}_j)) \cdot \exp\left(\|u(\mathbf{y}_j)\|^2 / \sigma_N^2\right). \end{aligned} \quad (13)$$

Here σ_N is a parameter that controls the range in searching for landmark correspondences.

Although multiple correspondences are allowed, it is shown in [Chui and Rangarajan, 2003] that the optimal correspondence for each landmark can be approximated by the expected mean displacement. As the result, we calculate the expected displacement $\bar{u}(\mathbf{p}) = \int u(\mathbf{p}) p(u|\mathbf{p}, \phi) du$ for each landmark and assign the landmark \mathbf{p} to its best correspondence candidate $\phi(\mathbf{p}) + \bar{u}(\mathbf{p})$ accordingly. Information of the selected landmarks and their correspondences will be utilized later for the estimation of the deformation field ϕ .

Updating the deformation field

The incremental deformation field $\Delta\phi$ is estimated from the incremental displacements \bar{u} by observing the following criteria:

1. The incremental deformation should reflect closely the updated landmark correspondences;
2. The incremental deformation field should be smooth.

To be precise, the incremental field $\Delta\phi$ is estimated by

$$\Delta\phi^* = \arg \min_{\Delta\phi} \sum_{i=1}^{N_c} \|\Delta\phi(\mathbf{x}_i) - \bar{u}(\mathbf{x}_i)\|^2 + \sum_{j=1}^{N_t} \|\Delta\phi(\mathbf{y}_j) - \bar{u}(\mathbf{y}_j)\|^2 + \text{Reg}(\Delta\phi). \quad (14)$$

Equation (14) aims to interpolate the dense field $\Delta\phi$ that approximates incremental displacements of all landmarks and satisfies the smoothness regularization $\text{Reg}(\Delta\phi)$ at the same time. In particular, $\Delta\phi$ can be obtained following

$$\Delta\phi \leftarrow G_{\Delta\phi} * \left(\sum_{i=1}^{N_c} \bar{u}(\mathbf{x}_i) + \sum_{j=1}^{N_t} \bar{u}(\mathbf{y}_j) \right), \quad (15)$$

where $G_{\Delta\phi}$ is a Gaussian kernel for imposing the smoothness constraint $\text{Reg}(\Delta\phi)$ and $*$ denotes the convolution operation [Vercauteren et al., 2009]. Other interpolation techniques including sophisticated basis functions (e.g., thin-plate-splines [Bookstein, 1989; Chui and Rangarajan, 2003]) are also applicable here.

After $\Delta\phi$ is computed, the overall deformation field is updated as $\phi \leftarrow \phi + \Delta\phi$. The updated deformation will be used to initiate a new iteration of correspondence detection. Although we have used a simple way to compose incremental deformations, other more sophisticated schemes can also be used, e.g., updating ϕ in the diffeomorphic setting by following $\phi \leftarrow \phi \circ \exp(\Delta\phi)$ [Vercauteren et al., 2009].

It is worth noting that the weighting factors for individual terms on the right sides of Eqs. (11) and (14) are intentionally ignored. The strength of the regularization term $\text{Reg}(\phi)$ or $\text{Reg}(\Delta\phi)$ can practically be controlled by specifying parameters for the Gaussian kernel $G_{\Delta\phi}$ in Eq. (15). To address the balance issue between contributions from the C-type and the T-type landmarks, we control the respective amounts of landmarks (i.e., N_c and N_t) instead of setting explicit weighting factors to $\text{Sim}_\times(\mathbb{X}, \phi)$ and $\text{Sim}_\vee(\mathbb{Y}, \phi)$ in Eq. (11). As in Wang et al. [2011], the connectivity features can provide more robust estimation of the deformation field especially in the early stages of DTI registration, while the tensor features are better utilized for subtle refinement to correspondence detection of landmarks in latter registration stages. To this end, we have empirically associated the amounts of landmarks, N_c and N_t , with the progress of registration. In particular, the number of C-type landmarks, or N_c , is high in the beginning. As registration proceeds, the ratio $N_c/(N_c + N_t)$ drops gradually while the contributions from the T-type landmarks, whose amount is N_t , are more emphasized. Note that the total amount of all landmarks (i.e., $N_c + N_t$) still increases according to “Selection of Landmarks” section when registration progresses, as more landmarks are necessary for accurate estimation of the deformation field especially when registration approaches completion.

We apply the multiresolution registration scheme in this work. Two different resolutions are used upon our data (i.e., size: $128 \times 128 \times 80$, spacing: $2 \times 2 \times 2 \text{ mm}^3$). The low-resolution deformation field is estimated from down-sampled DTI data, and then refined at the high resolution. Both connectivity features and tensor features are calculated only in the beginning of each resolution for the sake of computation cost. After warping the subject image to the template based on the estimated deformation field, the deformed tensors need to be re-orientated in relation to the deformation so that consistency of local connectivity pattern can be preserved. In particular, we use the tensor

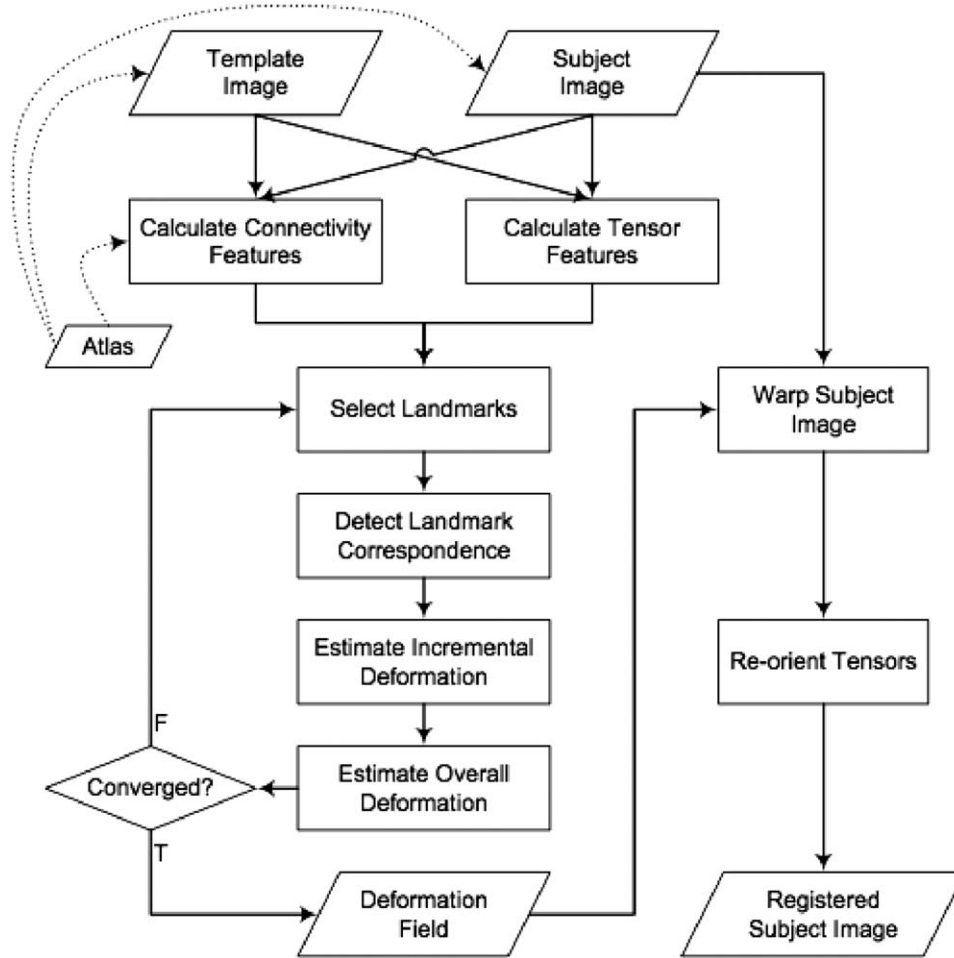


Figure 5.
Flowchart of the proposed method.

re-orientation algorithm that is reported in Xu et al. [2003]. It is worth noting that other methods [e.g., Alexander et al., 2001] for DT image warping could also be applied in this step.

Summary

We briefly summarize the proposed method as follows, with the flowchart in Figure 5:

1. Warp the atlas to the template and the subject images, respectively, to place the anchors;
2. Calculate the time arrival map with respect to each anchor, and generate the connectivity features for all voxels;
3. Calculate the tensor features for all voxels;
4. Select the set of landmarks, which will guide the estimation of the deformation field;
5. Update the correspondences for all landmarks;

6. Compute the incremental deformation field, and refine the overall deformation;
7. Loop from Step 4 until convergence, then output the deformation field;
8. Deform the subject image, and re-orient the deformed tensors accordingly.

Also, we provide several important parameters of our method in Table I. The first two parameters, including γ in Eq. (8) and the number of loops during the iterative optimization, will be further evaluated in the following experiments (“Synthetic Dataset” section). As discussed in “Estimation of the Deformation Field” section, we require balance between the strengths of the connectivity features and the tensor features by controlling \mathcal{N}_c and \mathcal{N}_t empirically. For each landmark, a locality constraint is introduced for the search of its correspondences such that a valid correspondence can only be acquired within the

TABLE I. Major parameters in the proposed method

Parameters	Low resolution	High resolution	Note
γ [Eq. (8)]	100	100	Regulate the number of anchors that contribute active connectivity features
Number of iterations $\mathcal{N}_c + \mathcal{N}_t$	12	12	Regulate the overall number of two types of landmarks
$\frac{\mathcal{N}_c}{(\mathcal{N}_c + \mathcal{N}_t)}$	Linearly and iteratively increase (20% of the brain volume in the first iteration, and 50% in the last)	Linearly and iteratively decrease (1.0 in the first iteration, and 0.0 in the last)	Regulate the ratio between the two types of landmarks
σ_N [Eq. (13)]	Linearly and iteratively decrease (7 voxels in the first iteration, and 1 voxel in the last)		Regulate the range for correspondence detection of landmarks
Sigma of $G_{\Delta\phi}$ [Eq. (15)]	Equal with σ_N		Regulate the kernel $G_{\Delta\phi}$ for the sake of the smoothness of $\Delta\phi$

radius of σ_N . The value of σ_N is initially high (at seven voxels in the first iteration of registration) and gradually decreases (to one voxel in the last iteration). The reasoning for this is that each landmark should become closer to its correspondence during the progression of image registration. The maximum search range for correspondence detection can be decreased accordingly. Similarly, the sigma of $G_{\Delta\phi}$, which regulates the smoothness of the incremental field as in Eq. (15), is defined to be equal with σ_N . In particular, we have followed the same setting as Yap et al. [2009] for σ_N and the sigma of $G_{\Delta\phi}$.

EXPERIMENTAL RESULTS

We applied the proposed method to both real and synthetic datasets and evaluated its performance. We also compared the new method with state-of-the-art approaches including DTI-TK [Zhang et al., 2006], F-TIMER [Yap et al., 2010] and our previous two-stage sequential registration method [Wang et al., 2011]. Among them, DTI-TK works on the tensor fields directly, with simultaneous consideration of tensor reorientation. F-TIMER utilizes tensor features to establish correspondences between voxels in the subject image and the template image. The sequential method divides the registration process into two stages, where the connectivity features and the tensor features are subsequently considered. In the proposed method, both types of features are simultaneously considered for DT image registration. Quantitative comparisons show that the proposed method yields substantially improved registration performance.

Real Dataset

We acquired 15 DT images for the use in validation (Siemens Allegra scanner, $b = 2,000$ s/mm², flip angle = 90°,

TR/TE = 13,649/82 ms, matrix 128×128 , FoV 256×256 mm², slice thickness 2 mm, 80 contiguous slices). Participants consisted of 10 male and 5 female healthy adults (age, 29.4 ± 3.2 years). All datasets were preprocessed by normalizing their FA maps to a common space via FLIRT [Jenkinson and Smith, 2001]. After selecting each image as the template in turn, we register all other 14 images to the template by using the methods listed above. Within each pair of template and registered images, we then calculated the in-between voxelwise tensor distances following the Log-Euclidean metric [Arsigny et al., 2006]. In particular, the distance between two tensors \mathbf{W}_1 and \mathbf{W}_2 is calculated by

$$\text{dist}(\mathbf{W}_1, \mathbf{W}_2) = \|\log \mathbf{W}_1 - \log \mathbf{W}_2\|_{\mathcal{F}}, \quad (16)$$

where $\|\cdot\|_{\mathcal{F}}$ indicates the matrix Frobenius norm. The average tensor distances in certain areas (i.e., white matter and gray matter) act as alignment accuracy indicators between DT images.

The average tensor distances associated with white matter and gray matter after registration by DTI-TK, F-TIMER, the sequential method, and the proposed method are listed in Table II. In white-matter area, the proposed method reduces the tensor distance by 9% compared with DTI-TK, 35% compared with F-TIMER, and 24% compared with the sequential method. Similarly, for gray matter, the proposed method reduces the tensor distance by 3%, 30%, and 20%, respectively. The decreases in average tensor distances are statistically significant ($p < 0.05$) when compared with either F-TIMER or the sequential method. The lowered tensor distance suggests that the proposed method is capable of achieving DTI registration with higher accuracy.

We further compute tract distances after registering the subject images with the template via individual methods. In particular, we manually delineated 18 major neural

TABLE II. Average tensor distances

	DTI-TK	F-TIMER	Sequential method	Proposed method
White matter	0.045 ± 0.007	0.063 ± 0.010	0.054 ± 0.009	0.041 ± 0.007
Gray matter	0.104 ± 0.013	0.145 ± 0.016	0.127 ± 0.016	0.101 ± 0.015

tracts shared among the images and then compared the distances between pairs of tracts in the template as well as for each warped subject. We apply the tractography method known as FACT [Jiang et al., 2006] for fiber tracking. Fibers passing through certain regions of interest (ROIs) are grouped and compared. The seeding threshold of FA in fiber tracking is 0.3, while fibers terminate at the FA threshold 0.2. A maximum turning angle of 30° is allowed. All fibers are restricted to the length range 40–400 mm. ROIs for tract extraction are drawn manually in the template space. Examples of tracts from the template, a randomly selected subject before registration, and the subject after registration via the proposed method are annotated in Figure 6, respectively. Note that only tracts on the right hemisphere are shown for convenience. For the subject prior to registration, the ROIs are transferred from the template to its own space, for the sake of tract extraction, by registering the FA maps of the two images. The tract distance is then defined as

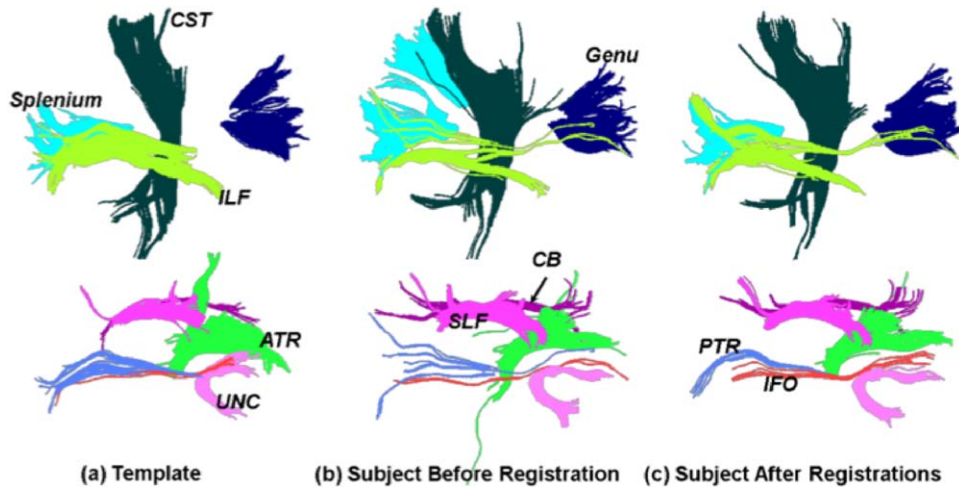
$$\frac{1}{|\mathcal{A}|+|\mathcal{B}|} \left[\sum_{\mathcal{A}_i \in \mathcal{A}} \min_{\mathcal{B}_j \in \mathcal{B}} \text{dist}(\mathcal{A}_i, \mathcal{B}_j) + \sum_{\mathcal{B}_i \in \mathcal{B}} \min_{\mathcal{A}_j \in \mathcal{A}} \text{dist}(\mathcal{B}_i, \mathcal{A}_j) \right], \quad (17)$$

where \mathcal{A} and \mathcal{B} indicate the fiber bundles extracted from the template and subject images, respectively, and

$\text{dist}(\mathcal{A}_i, \mathcal{B}_j)$ is a pairwise distance between fibers $\mathcal{A}_i \in \mathcal{A}$ and $\mathcal{B}_j \in \mathcal{B}$. The pairwise distance between fibers is defined as the mean of the closest distance for every point of two fibers [Gerig et al., 2004]. The tract distances averaged over all subjects yield by the four registration methods are plotted in Figure 7. Among all 18 bundles, the proposed method achieves the lowest residual tract distance in 14 tracts. The overall distances for the proposed method, DTI-TK, F-TIMER, and the sequential method are 1.451 mm, 1.824 mm, 1.608 mm, and 1.511 mm, respectively.

Synthetic Dataset

We further evaluated the performance of the proposed method on a synthetic dataset and gauged its accuracy in estimating the deformation fields. In particular, we warp the FA map of a randomly selected image from “Real Dataset” section onto another FA map via scalar image registration (i.e., FLIRT [Jenkinson and Smith, 2001] followed by diffeomorphic Demons [Vercauteren et al., 2009]) in order to acquire a real deformation. The deformation field, which acts as the ground truth for evaluation, deforms the selected DT image to generate the realistic synthetic dataset. To evaluate alignment accuracy in DTI registration, we register the original selected image to the

**Figure 6.**

Exemplar tracts for comparing images of (a) the template, (b) a randomly selected input subject, and (c) the warped subject after registration via the proposed methods. [Color figure can be viewed in the online issue, which is available at wileyonlinelibrary.com.]

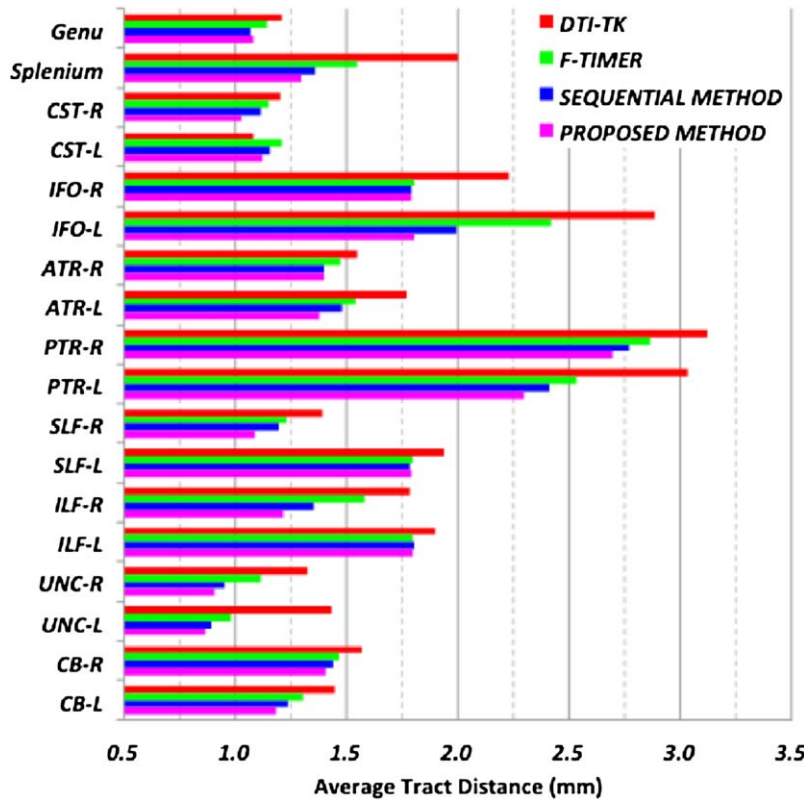


Figure 7.

Average tract distances between registered subjects and the template for 18 manually delineated neural tracts. [Color figure can be viewed in the online issue, which is available at wileyonlinelibrary.com.]

simulated image that acts as template. The estimated deformation field by different registration methods can then be compared to the ground truth. We run the procedure above for 15 times and test individual registration methods on all cases. Note that our approach of simulation and evaluation avoids the potential errors involved in the inversion of deformation fields as in Wang et al. [2011].

Representative registration results yielded by the proposed method are shown in Figure 8, where Figure 8A extracts six consecutive slices from the FA map of a selected image as subject. Figure 8B,C show corresponding FA slices from the synthetic template and the deformed subject after DTI registration via the proposed method, respectively. By comparing Figure 8B,C, we can conclude that the proposed method produces good structural alignment as the registration output is visually very close to the template image. Comparison of the ground-truth deformation field in Figure 8D with the deformation field estimated by the proposed method in Figure 8E gives a similar conclusion.

We also performed a quantitative evaluation on the registration accuracy by calculating the residual errors between the estimated deformation fields and the ground-

truth deformation fields. Specifically, we compute the deformation errors for all cases with respect to 12 white-matter regions that are associated with major fiber bundles. The average residuals are plotted in Figure 9. For all regions, the proposed method has achieved lower errors than DTI-TK, F-TIMER and the sequential method. The overall deformation error given by the proposed method is 0.57 mm, lower than 1.00 mm given by DTI-TK, 0.92 mm given by F-TIMER, and 0.65 mm given by the sequential method.

Our experiments indicate that connectivity features and tensor features are complementary for improving registration accuracy. After disabling tensor features (i.e., by arbitrarily setting \mathcal{N}_t to 0), we are able to count contributions from connectivity features only. The resulted errors of the deformation fields are listed as CONN-DEMONS in Figure 9. Note that F-TIMER utilizes tensor features only. We can conclude from Figure 9, however, that the accuracies of F-TIMER and CONN-DEMONS are very similar. The overall deformation error given by CONN-DEMONS is 0.93 mm, close to F-TIMER yet much worse than the proposed method. Though neither F-TIMER nor CONN-DEMONS yields superior results independently, the accuracy of DTI registration by utilizing the combinations of connectivity

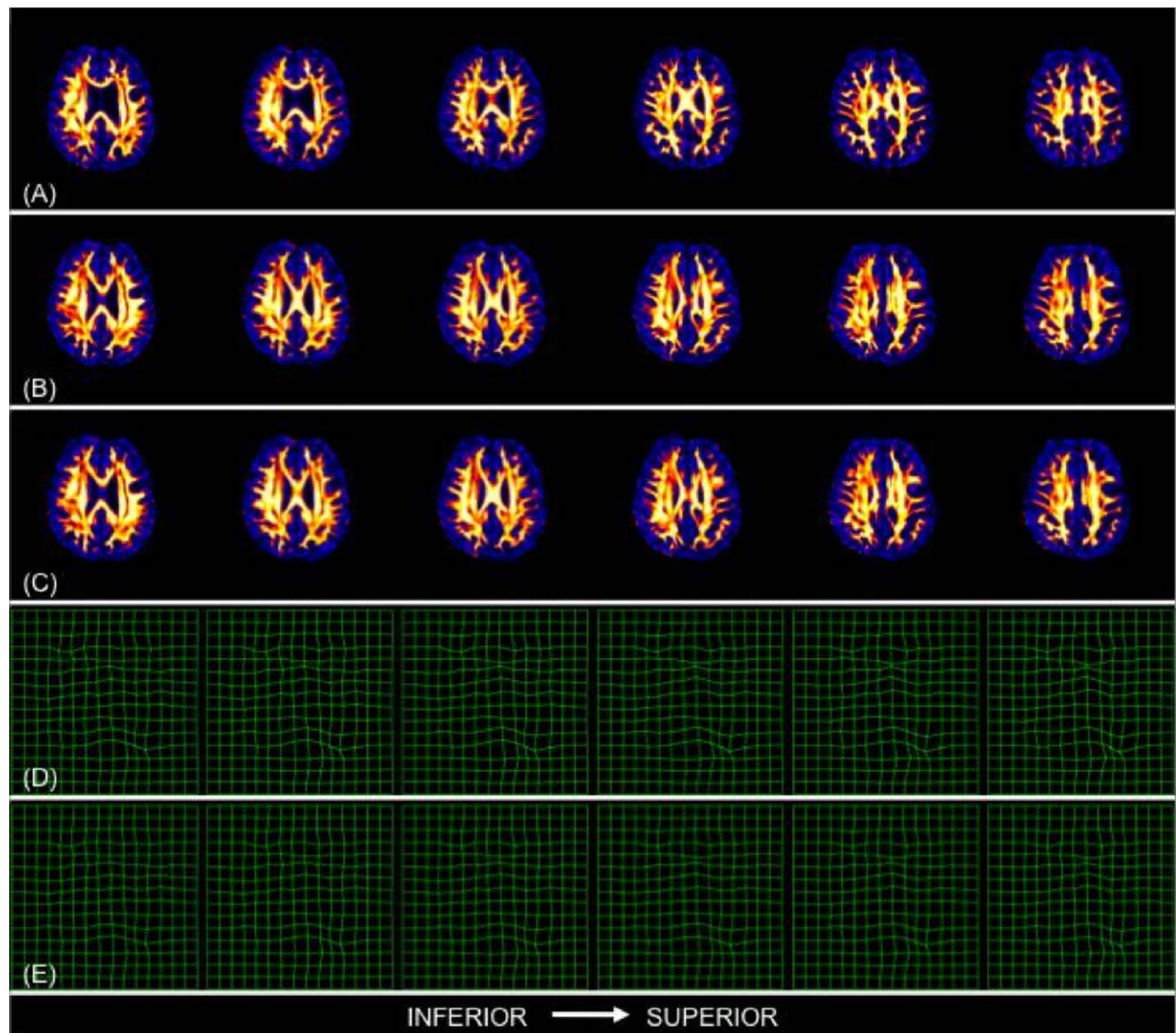


Figure 8.

FA slices from the subject (A), the template (B), and the results produced by the proposed method (C) using the deformation field shown in (E). For comparison, the ground-truth deformation field is shown in (D). [Color figure can be viewed in the online issue, which is available at wileyonlinelibrary.com.]

features and tensor features in a proper manner (i.e., the proposed method in Fig. 9) has increased significantly.

We also verified the influence of anchor placement to the calculation of the connectivity features and thus the registration performance. The template-subject correspondences between pairs of anchors are important as the fundamentals for C-type landmarks to establish their own correspondences. Usually, we align the atlas to the template/subject via FLIRT [Jenkinson and Smith, 2001] and diffeomorphic Demons [Vercauteren et al., 2009], which is adopted by CONN-DEMONS, the sequential method, and

the proposed method. For comparison, we align the atlas to both the template and subject spaces via FLIRT [Jenkinson and Smith, 2001] yet without deformable registration, and then count contributions from connectivity features only. The resulted errors of the deformation fields are listed as *CONN-AFFINE* in Figure 9. Compared with CONN-DEMONS, the accuracy of CONN-AFFINE locates at a comparable level with the overall error 0.95 mm, even though correspondences between pairs of anchors in template and subject could be more reliable overall in CONN-DEMONS than CONN-AFFINE. These results imply that

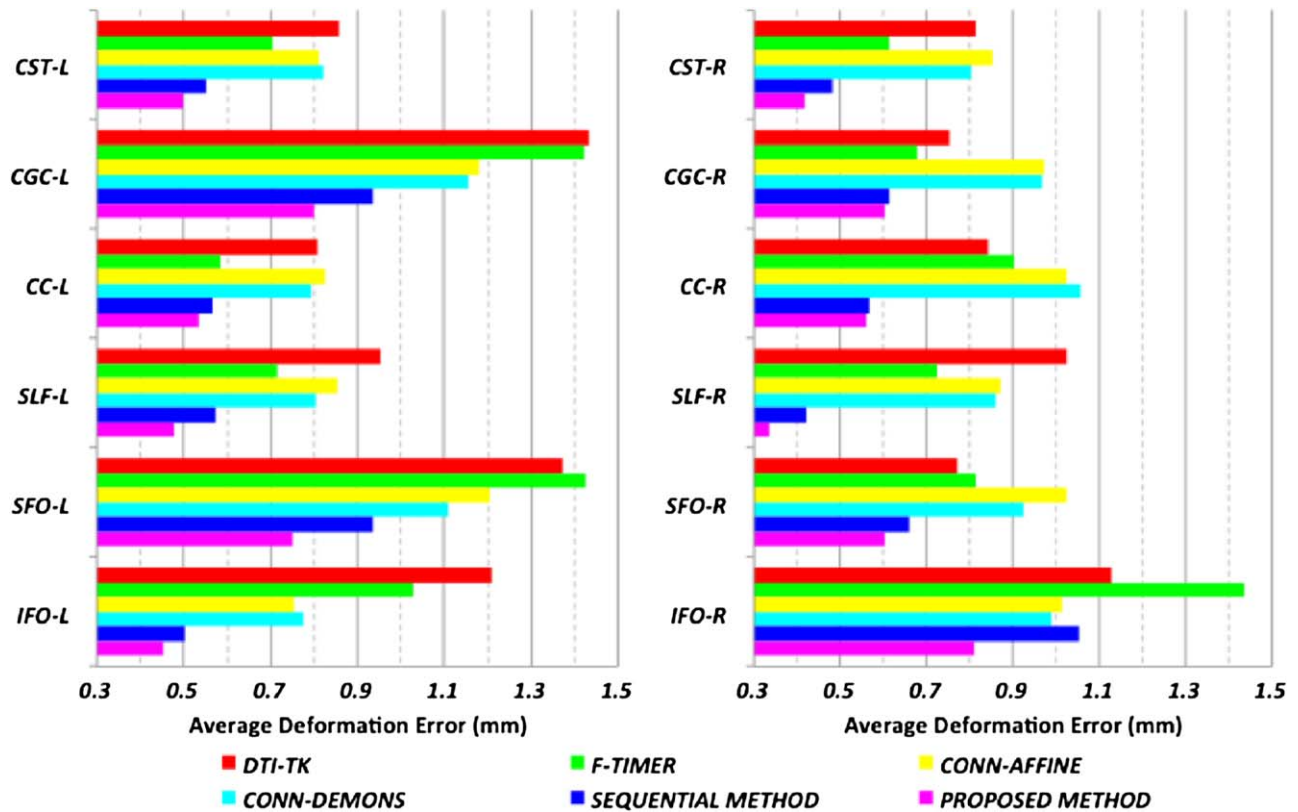


Figure 9.

Average residual errors of the estimated deformation fields, compared with the ground-truth deformation fields, in 12 white-matter regions that are associated with major fiber bundles. [Color figure can be viewed in the online issue, which is available at wileyonlinelibrary.com.]

the adaptive weighting strategy associated with connectivity features can select anchors with high confidences automatically, thus alleviating reliability issues with the connectivity features.

We performed additional evaluation by computing the deformation errors associated with the landmarks, which essentially steer the registration. We define three sets of landmarks: Set 1 contains C-type landmarks; Set 2 contains T-type landmarks sampled from FA edges; and Set 3 contains T-type landmarks sampled from tensor edges. The errors between the estimated deformations of landmarks and their ground-truth deformations are listed in Table III. The proposed method yields lower ($p < 0.05$) deformation errors compared with DTI-TK, F-TIMER, and the sequential method for all selected landmarks.

By utilizing the residual deformation errors measured from the synthetic dataset, we are further able to verify the determination of γ and the number of iterations, both of which are important parameters in the proposed method. In Figure 10, for illustration, we plot the overall error averaged from all regions listed in Figure 9 for various numbers of iterations. The results indicate that the residual deformation error gradually reduces when more iterations are allowed for optimization, stabilizing around 12 iterations. Therefore, the number of iterations is set as 12 for our method.

The number of active anchors, which is controlled by the parameter γ , plays a vital role in determining the performance of our method. In Figure 11, we adjust the value of γ and plot the remaining number of active anchors as

TABLE III. Deformation errors (unit: mm) for three different sets of landmarks

Landmarks	DTI-TK	F-TIMER	Sequential method	Proposed method
Set 1	1.159 ± 0.190	0.923 ± 0.140	0.527 ± 0.118	0.437 ± 0.106
Set 2	1.173 ± 0.218	1.005 ± 0.179	0.695 ± 0.156	0.505 ± 0.178
Set 3	1.177 ± 0.284	0.978 ± 0.232	0.541 ± 0.117	0.502 ± 0.133

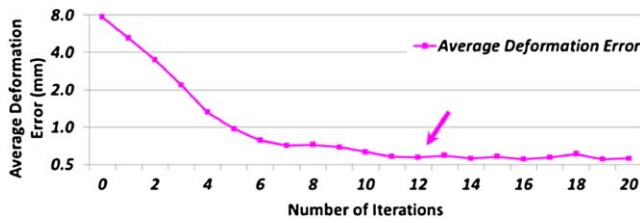


Figure 10.

The average residual error between the estimated deformation fields and the ground truth, in 12 white-matter regions, changes according to different numbers of iterations used in the proposed method. [Color figure can be viewed in the online issue, which is available at wileyonlinelibrary.com.]

well as the average deformation error. Specifically, we set γ to 100 in our method, as the lowest deformation error is most likely to be achieved. We conclude from Figure 11 that the number of active anchors can be reduced to $\sim 10\%$ of the total number of anchors. It is worth noting that the error of the deformation fields drops drastically when γ slightly deviates from 0 (i.e., $\gamma=1$). In fact, with $\gamma=0$, there is no selection of the active anchors, meaning that incorrectly placed anchors (i.e., anchors in low-FA areas) will undermine the registration performance. However, for any positive γ (i.e., $\gamma=1$), the mechanism that selects active anchors starts to work and rejects these obviously wrong anchors immediately. By increasing γ , higher sparsity of the active anchors is favored such that the number of active anchors further drops. In general, we observe the lowest deformation error in the vicinity of $\gamma=100$ for our method.

CONCLUSION AND DISCUSSION

In this article, we have proposed a novel method for DTI registration that unifies both connectivity and tensor

features. The connectivity features take advantage of the tensor field to characterize each voxel and its relationship with preplaced anchors. The tensor features focus more on the appearance of tensors and capture the local statistics for each voxel in its neighborhood. The two types of features are complementary, and both benefit registration by providing reliable ways to identify voxelwise correspondences. After selecting landmarks that are crucial to registration, we collect their correspondence information based on their connectivity/tensor features and optimize the deformation field between the two images iteratively. The moving subject image is warped to the template space following the estimated deformation field, with the deformed tensors re-oriented afterward to preserve local connectivity consistency. Our experimental results confirm that the accuracy in DTI registration has been improved significantly by using connectivity features and tensor features simultaneously.

Tensor features reflect *local* characteristics of each voxel, while connectivity features depict the relationship between each voxel and remote anchors, providing a *nonlocal* means of describing the voxel under consideration. Voxel similarity based on connectivity features is directly related to the accuracy of anchor placement. In the early stages of registration, landmarks are possibly far away from their true correspondences and have to search within wide neighborhoods. In this case, correspondence detection is difficult using locally defined tensor features, and the nonlocal connectivity features are more robust in estimating the desired displacement for each landmark. As registration progresses to the end, however, we focus more on tensor features—the confidences of correspondences between anchors may restrict connectivity features to sustain granulated refinement in late correspondence detection.

We apply the fast marching method to compute connectivity features. The resulting geodesic distance, however, is asymmetric due to numerical errors. In other words, the computed distance from voxel a to b could be slightly

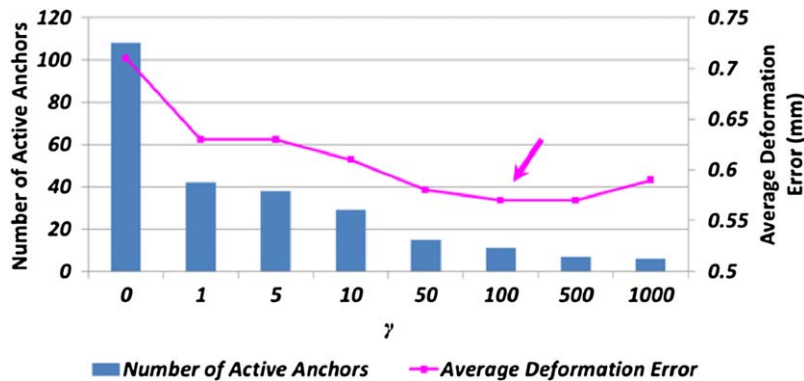


Figure 11.

The average residual error between the estimated deformation fields and the ground truth, as well as the number of active anchors, changes according to γ . [Color figure can be viewed in the online issue, which is available at wileyonlinelibrary.com.]

different from the distance from b to a . This issue is also reflected in Eqs. (6)–(8) during the estimation of the confidences between individual pairs of anchors. We define the connectivity features for each voxel as the distances from anchors to the voxel under consideration. In this way, we only need to calculate the time arrival maps that are associated with all anchors. We can expedite the computation of connectivity features via parallelization.

Connectivity features, as well as tensor features, contribute to correspondence detection for landmarks and estimation of the final deformation field. It is thus critical to accurately compute voxel features for registration performance. In particular, we expect high confidence of the correspondence between a specific pair of anchors in the template and the to-be-registered subject. To this end, we have introduced a strategy that adaptively weights individual entries in the connectivity feature vector when comparing the similarity of two voxels. Only a limited number of active anchor pairs are assigned with non-zero confidences and preserved for image registration. We assume the confidence of the placement of an individual pair of anchors is independent of the confidence for every other pair. Thus, any two anchor pairs can be treated independently in computing the connectivity features for individual voxels. Our assumption is based on the following observations:

1. Using deformable registration, the placement error associated with each anchor can be propagated to a neighborhood of limited size. However, our anchors that signify anatomical areas are not closely located with others in general. Since the anchors are relatively sparse (108 anchors vs. hundreds of thousands of voxels) and well-separated in space, their mutual effect can be safely neglected.
2. An anchor is calculated as the gravity center of an associated warped ROI. Therefore, the accuracy in placing an anchor is not directly correlated with the accuracy in placing an entire ROI. For example, given a well-placed ROI, the corresponding anchor could still be possibly placed in a low-FA area and then excluded from contributing to the registration. As the result, it is nonevident to conclude that even the reliabilities of neighboring anchors are highly related.
3. Our experiments indicate that the proposed method is robust to reasonable accuracy in placing the anchors. For example, we have tried using both affine registration (i.e., FLIRT) and nonrigid registration (i.e., Diffeomorphic Demons) for warping the atlas to the template/subject space. The two methods differ significantly in terms of registration accuracy; however, using the anchors placed by these different methods, the performance of our method does not differ significantly.

We currently control the strengths of connectivity features and tensor features empirically, as the numbers of C-type and T-type landmarks are associated with the itera-

tive progress of registration. The scheme is partly based on our previous work in Wang et al. [2011] and show improved registration performances according to the experiments. Since we arbitrary select the proportion of C-type and T-type landmarks, a better, yet more complicated, approach might be to allow automated allocation of the number of landmarks for each type of feature.

Currently, we evaluate the performance of our method on normal adult data only, as the demographic information is provided in “Real Dataset” section. It would be interesting to evaluate our method using images from patients who are suffering from neurodegenerative disorders. Since the proposed method leverages the hybrid of local tensor and global connectivity information, we believe it will help improve alignment of images with large anatomical differences. However, we note that our method might be affected by the alteration of connectivity patterns associated with the disorders. Further investigation is thus required to evaluate how changes in connectivity affect registration. Another shortcoming of our method, in our opinion, lies in the fact that the reorientation of tensors is not explicitly included in the optimization process. In the future, it would be interesting to study how explicit reorientation optimization improves the performance of our method.

ACKNOWLEDGMENTS

This work was supported by the NIH grants EB006733, EB008374, EB009634, AG041721, MH100217, and AG042599, and the National Research Foundation grant 2012-005741 from the Korea government.

REFERENCES

- Alexander DC, Gee JC (2000): Elastic matching of diffusion tensor images. *Comput Vis Image Understand* 77:233–250.
- Alexander DC, Pierpaoli C, Basser PJ, Gee JC (2001): Spatial transformations of diffusion tensor magnetic resonance images. *IEEE Trans Med Imaging* 20:1131–1139.
- Arsigny V, Fillard P, Pennec X, Ayache N (2006): Log-Euclidean metrics for fast and simple calculus on diffusion tensors. *Magn Reson Med* 56:411–421.
- Baerentzen JA (2001): On the Implementation of Fast Marching Methods for 3D Lattices. *Informatics and Mathematical Modeling*, Technical Report IMM-REP-2001-13, Technical University of Denmark.
- Basser PJ, Mattiello J, LeBihan D (1994): MR diffusion tensor spectroscopy and imaging. *Biophys J* 66:259–267.
- Bookstein FL (1989): Principal warps: Thin-plate splines and the decomposition of deformations. *IEEE Trans Pattern Anal Mach Intell* 11:567–585.
- Chiang MC, Leow AD, Klunder AD, Dutton RA, Barysheva M, Rose SE, McMahon KL, de Zubicaray GI, Toga AW, Thompson PM (2008): Fluid registration of diffusion tensor images using information theory. *IEEE Trans Med Imaging* 27:442–456.
- Chui H, Rangarajan A (2003): A new point matching algorithm for non-rigid registration. *Comput Vis Image Understand* 89: 114–141.

- Gee JC, Alexander DC (2006): Diffusion-tensor image registration. In: Weickert J, Hagen H, editors. *Visualization and Processing of Tensor Fields*. Berlin, Heidelberg: Springer. pp 327–342.
- Gerig G, Gouttard S, Corouge I (2004): Analysis of brain white matter via fiber tract modeling. *Conf Proc IEEE Eng Med Biol Soc* 6:4421–4424.
- Goodlett C, Davis B, Jean R, Gilmore J, Gerig G (2006): Improved Correspondence for DTI Population Studies via Unbiased Atlas Building. In *Medical Image Computing and Computer-Assisted Intervention–MICCAI 2006*, pp. 260–267. Springer Berlin Heidelberg, 2006.
- Guimond A, Guttman CRG, Warfield SK, Westin CF (2002): Deformable Registration of DT-MRI Data Based on Transformation Invariant Tensor Characteristics. *ISBI*. pp 761–764.
- Hassouna MS, Farag AA (2007): Multistencils fast marching methods: A highly accurate solution to the Eikonal equation on Cartesian domains. *IEEE Trans Pattern Anal Mach Intell* 29: 1563–1574.
- Ingallhalikar M, Yang J, Davatzikos C, Verma R (2010): DTI-DROID: Diffusion tensor imaging-deformable registration using orientation and intensity descriptors. *Int J Imag Syst Technol* 20:99–107.
- Irfanoglu MO, Machiraju R, Sammet S, Pierpaoli C, Knopp MV (2008): Automatic deformable diffusion tensor registration for fiber population analysis. In *Medical Image Computing and Computer-Assisted Intervention–MICCAI 2008*, pp. 1014–1022. Springer Berlin Heidelberg, 2008.
- Jenkinson M, Smith S (2001): A global optimisation method for robust affine registration of brain images. *Med Image Anal* 5: 143–156.
- Jia H, Yap PT, Wu G, Wang Q, Shen D (2011): Intermediate templates guided groupwise registration of diffusion tensor images. *NeuroImage* 54:928–939.
- Jiang H, van Zijl PC, Kim J, Pearlson GD, Mori S (2006): DtiStudio: Resource program for diffusion tensor computation and fiber bundle tracking. *Comput Methods Programs Biomed* 81: 106–116.
- Li H, Xue Z, Guo L, Wong SC (2009): Simultaneous consideration of spatial deformation and tensor orientation in diffusion tensor image registration using local fast marching patterns. In: Prince J, Pham D, Myers K, editors. *Information Processing in Medical Imaging*. Berlin, Heidelberg: Springer. pp 63–75.
- Mori S, van Zijl PC (2002): Fiber tracking: Principles and strategies—a technical review. *NMR Biomed* 15:468–480.
- Mori S, Oishi K, Jiang H, Jiang L, Li X, Akhter K, Hua K, Faria AV, Mahmood A, Woods R, Toga AW, Pike GB, Neto PR, Evans A, Zhang J, Huang H, Miller MI, van Zijl P, Mazziotta J (2008): Stereotaxic white matter atlas based on diffusion tensor imaging in an ICBM template. *Neuroimage* 40:570–582.
- Park HJ, Kubicki M, Shenton ME, Guimond A, McCarley RW, Maier SE, Kikinis R, Jolesz FA, Westin CF (2003): Spatial normalization of diffusion tensor MRI using multiple channels. *Neuroimage* 20:1995–2009.
- Rohde GK, Pajevic S, Pierpaoli C, Basser PJ (2003): A comprehensive approach for multi-channel image registration. *Biomedical image registration*. Berlin/Heidelberg: Springer. pp 214–223.
- Ruiz-Alzola J, Westin CF, Warfield SK, Alberola C, Maier S, Kikinis R (2002): Nonrigid registration of 3D tensor medical data. *Med Image Anal* 6:143–161.
- Sethian JA (1996): A fast marching level set method for monotonically advancing fronts. *Proc Natl Acad Sci USA* 93:1591–1595.
- Shen D, Wong WH, Ip HH (1999): Affine-invariant image retrieval by correspondence matching of shapes. *Image and Vision Computing* 17:489–499.
- Siless V, Glaunès J, Guevara P, Mangin J-F, Poupon C, Bihan D, Thirion B, Fillard P (2012): Joint T1 and brain fiber log-demons registration using currents to model geometry. In: Ayache N, Delingette H, Golland P, Mori K, editors. *Medical Image Computing and Computer-Assisted Intervention (ICCAI 2012)*. Berlin, Heidelberg: Springer. pp 57–65.
- van Hecke W, Leemans A, D’Agostino E, de Backer S, Vandervliet E, Parizel PM, Sijbers J (2007): Nonrigid coregistration of diffusion tensor images using a viscous fluid model and mutual information. *IEEE Trans Med Imaging* 26:1598–1612.
- Vercateren T, Pennec X, Perchant A, Ayache N (2009): Diffeomorphic demons: Efficient non-parametric image registration. *Neuroimage* 45:S61–S72.
- Verma R, Davatzikos C (2004): Matching of diffusion tensor images using Gabor features. *IEEE Int Symp Biomed Imag: Nano Macro* 391:396–399.
- Wang Q, Wu G, Yap PT, Shen D (2010): Attribute vector guided groupwise registration. *Neuroimage* 50:1485–1496.
- Wang Q, Yap PT, Wu G, Shen D (2011): Diffusion Tensor Image Registration with Combined Tract and Tensor Features. In *Medical Image Computing and Computer-Assisted Intervention–MICCAI 2011*. pp. 200–208. Springer Berlin Heidelberg, 2011.
- Wang Q, Yap PT, Wu G, Shen D: Application of neuroanatomical features to tractography clustering. *Hum Brain Mapp* (in press).
- Wu G, Qi F, Shen D (2006): Learning-based deformable registration of MR brain images *Medical Imaging, IEEE Transactions on* 25:1145–1157.
- Xu D, Mori S, Shen D, van Zijl PC, Davatzikos C (2003): Spatial normalization of diffusion tensor fields. *Magn Reson Med* 50: 175–182.
- Yan C, Miller MI, Mori S, Winslow RL, Younes L (2006): Diffeomorphic matching of diffusion tensor images. In: *Conference on Computer Vision and Pattern Recognition Workshop, CVPRW ’06*. pp 67–67.
- Yang J, Shen D, Davatzikos C, Verma R (2008): Diffusion tensor image registration using tensor geometry and orientation features. *MICCAI*. pp 905–913.
- Yap PT, Wu G, Zhu H, Lin W, Shen D (2009): TIMER: Tensor image morphing for elastic registration. *Neuroimage* 47:549–563.
- Yap PT, Wu G, Zhu H, Lin W, Shen D (2010): F-TIMER: Fast tensor image morphing for elastic registration. *IEEE Trans Med Imaging* 29:1192–1203.
- Yeo BTT, Vercateren T, Fillard P, Pennec X, Gotland P, Ayache N, Clatz O (2008): DTI Registration with Exact Finite-Strain Differential. In *Biomedical Imaging: From Nano to Macro, 2008. ISBI 2008. 5th IEEE International Symposium on* pp 700–703.
- Zacharaki EI, Shen D, Lee SK, Davatzikos C (2008): ORBIT: a multiresolution framework for deformable registration of brain tumor images. *Medical Imaging, IEEE Transactions on* 27:1003–1017.
- Zhang H, Yushkevich PA, Alexander DC, Gee JC (2006): Deformable registration of diffusion tensor MR images with explicit orientation optimization. *Med Image Anal* 10:764–785.
- Ziyan U, Sabuncu MR, O’Donnell LJ, Westin CF (2007): Nonlinear registration of diffusion MR images based on fiber bundles. *MICCAI*. pp 351–358.